Tuning the properties of NBR/BaFe$_{11.5}$Co$_{0.5}$O$_{19}$: a road toward diverse applications

Ebtesam E. Ateia[1] · Kareem Elsayed[1] · D. E. El-Nashar[2]

Abstract

The present work aims to synthesize and designate 50% BaFe$_{11.5}$Co$_{0.5}$O$_{19}$ /50% NBR nanocomposite with enhanced physical properties. First, the BaFe$_{11.5}$Co$_{0.5}$O$_{19}$ hexaferrite was successfully synthesized by the citrate auto-combustion technique. Composite nanoparticles were synthesized by melt mixing technique in a Brabender Plasticorder. The structure and morphology of the samples were investigated using X-ray diffraction (XRD), Fourier transform infrared (FTIR), Raman spectroscopy, X-ray photoelectron spectroscopy, atomic force microscopy (AFM), and scanning electron microscope (SEM). The average crystallite size is nearly 35 nm. The high values of Ms for BFCO can be clarified by Fe^{3+}–O–Fe^{3+} super-exchange interaction in the present system. An investigation has found that substitution in M-type hexaferrite systems alters the valence states of Fe^{3+} ions to Fe^{3+} ions at the 2A sites (Ateia et al. in Appl Phys A 128: 884, 2022). This causes an enhancement of super-exchange interactions that improves the hyperfine field at 2b and 12 k sites. The switching field distribution was computed and reported. Tensile strength (T.S), Young's modulus (E), hardness (H) and Rheometric characteristics were enhanced after the addition of BFCO nanoparticles to NBR polymer. The obtained data from the present study revealed that the incorporation of 50% of BaFe$_{11.5}$Co$_{0.5}$O$_{19}$ hexaferrite with 50% of NBR rubber enhanced the physico-mechanical and magnetic characteristics of the prepared composites. This indicates that hexaferrites achieve not only appropriate magnetic properties for the prepared composites, but also strengthen the rubber matrix. The originality of this investigation is clarified by emphasizing the magnetization of NBR and to accentuate the good mechanical properties of the investigated nanocomposites.

Keywords Hexaferrite · Magnetization of NBR · Nanocomposites · Switching field distribution · Effective anisotropy constant

1 Introduction

Nanocomposites are increasingly being studied for their properties, particularly those with unique features. Rubber ferrite composites (RFCs) are an example of a material with exceptional properties. Composites are created by incorporating ferrite fillers into natural and synthetic rubber matrices. [1] Ferrites are types of magnetic materials with a wide range of technological applications such as transformer cores, memory storage devices, circulators, and a variety of other recent devices that cannot be easily replaced by other materials due to their stability, high electrical resistivity, economy, and so on [2]. One of the ferromagnetic materials with distinct magnetic characteristics is BaFe$_{12}$O$_{19}$, which belongs to the M-hexaferrite (HF) group. Its crystal structure belongs to the P6$_3$/mmc space group and is made up of alternate layers of hexagonal (R) and spinel (S) layers, and the layers have the sequences of SRS*R*. Similar to S and R, the S* and R* layers are S and R with the c-axis rotated 180 degrees. As illustrated in Fig. 1 [3], one unit cell of M-hexaferrite contains 38 O^{2-} ions, two Ba^{2+} ions, and 24 Fe^{3+} ions.

Due to its potential uses in a wide range of electrical and microwave devices, barium hexaferrite is one of the most significant groups of materials in the permanent magnet family. Because of its high coercivity, remanent magnetization, high magneto-crystalline anisotropy, and large spontaneous

✉ Ebtesam E. Ateia
drebtesam2000@yahoo.com; ebtesam@sci.cu.edu.eg

✉ Kareem Elsayed
kareemelsayed@cu.edu.eg

[1] Physics Department, Faculty of Science, Cairo University, Giza, Egypt

[2] Polymers and Pigments, National Research Centre, Dokki, Cairo, Egypt

Fig. 1 The unit cell and spin configurations for $BaFe_{12}O_{19}$ are as follows: Ba, O, and Fe atoms are represented by purple, red, and gold spheres, respectively. The arrows show the atom's local magnetic moment
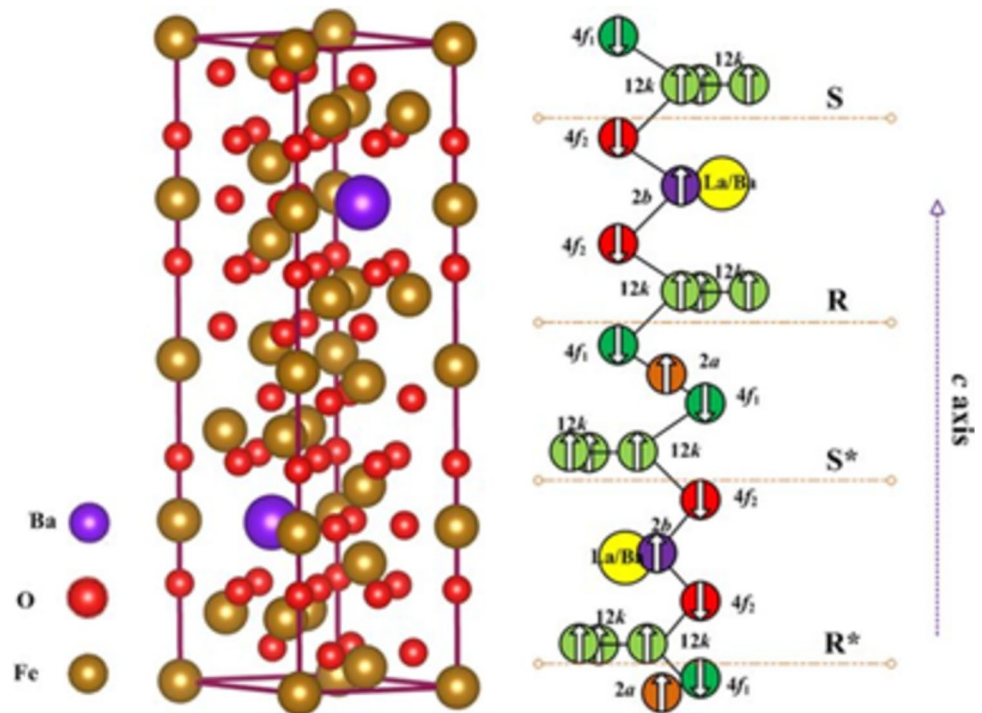
polarization, it has attracted the most commercial interest [4].

When ferrite fillers are mixed into a rubber matrix, they modify the elastomer's mechanical, magnetic, and other physical characteristics. The flexibility and moldability of RFCs as microwave absorbers and electromagnetic interference (EMI) shielding materials are important [5]. When a suitable polymer matrix is selected, ferrite filler may be included to create a composite with the required magnetic, and mechanical characteristics. Various rubbers, such as natural rubber (NR), acrylonitrile butadiene rubber (NBR), styrene butadiene rubber (SBR), and ethylene propylene diene monomer (EPDM), are widely used in the preparation of such RFCs [6]. Moreover, NBR is a member of a large family of unsaturated copolymers comprising acrylonitrile and butadiene. It belongs to a group of rubbers that are flexible at low temperatures, resistant to aging, and resistant to water, oils, and solvents.

Polymer magnetic nano-composite materials are a group of smart materials consisting of ferrite magnetic materials combined with a conductive polymer matrix [6–8]. The final properties of nanocomposites are strongly dependent on the characteristics of the ferrite/polymer matrix. However, by applying ferrite magnetic materials with polymer compounds through processing technologies, new properties and technological abilities can be provided. The advantage of such nanocomposites is that their properties can be adapted to the requirements of numerous applications. They are suitable for additive devices because of their elasticity and easy moldability, where elasticity and flexibility are important additional

properties. Ferrite/rubber nanocomposites are able to sensitively respond to vibrations and absorb oscillations of various wavelengths [9].

They can also change magnetic and mechanical properties at different levels of strain. The tunable properties of ferrite/polymer nanocomposites can be achieved by selecting suitable magnetic materials and their concentrations. Conductive polymers, such as NBR, magnetic materials, especially hexaferrite, can be used as efficient EMI shielding materials and have numerous other applications [5].

In this study, rubber magnetic nanocomposites were prepared by mixing magnetic NPs of BFCO with NBR as polar rubber matrices. The physico-mechanical characteristics of the prepared composites were examined. The main goal is to improve the mechanical and magnetic properties of the prepared samples.

2 Methodology

2.1 Material used

All chemicals Ba $(NO_3)_3 \cdot 6H_2O$ (99%), Co (NO3)·0.6H$_2$O, Fe $(NO_3)_3 \cdot 6H_2O$ (98%), and citric acid [$C_4H_8O_7$], and ammonia solution (33%) were obtained from (LOBA, India).

2.2 Experimental technique

2.2.1 Preparation of ferrite samples

The citrate auto-combustion technique was used to create nanoparticles of cobalt-doped Barium hexaferrite. The proper quantities of the precursors were added to match the stoichiometric ratios of nitrates. These precursors were combined with citric acid by adding distilled water dropwise while vigorously stirring. The pH was then adjusted to 7, and the temperature was elevated to 200 °C until all fumes were eliminated, as illustrated in (Fig. 2a).

2.2.2 Preparation on NBR samples

NBR was selected as the rubber matrix. A laboratory two-roll mill was used for mixing (470 mm diameter and 300 mm working distance). According to ASTM D3182-07, the slow roll has a speed of 24 rev/min and a gear ratio of 1:1.4. The two rolls were mildly heated to soften the elastomer matrix and facilitate mastication. Following the mastication process, additives (ferrite) were introduced to the elastomer matrix and homogenized using the two roll-mixing mills.

2.2.3 Nanocomposite preparation

The investigated nanocomposite of 50% NBR/50% BaFe$_{11.5}$Co$_{0.5}$O$_{19}$ was created using a Melt mixing process in a Brabender Plasticorder [1], as shown in Fig. 2b. For the optimal cure time, the nanocomposite was vulcanized in an electrically heated hydraulic press at 162 °C and a pressure of around 4 MPa (tc 90 min).

2.2.4 Rheometric characteristics

The complete "Cure Curve" is produced as mentioned in the previous work [6]. This behavior is shown in Fig. 2c.

The M$_L$ is torque with the lowest recorded value, M$_H$ is the maximum torque measured in the plateau curve, ts$_2$ is the time necessary to reach 2 units above ML, indicating the time required to begin the process of cross-linking, tc$_{90}$ is the time at which 90% of the cure has occurred, and CRI is the rate at which the compound's cross-linking and stiffness (modulus) grow after the scorch point

$$CRI = \frac{100}{(tc_{90} - ts_2)} \qquad (1)$$

Phase 1: It describes how the rubber compound is processed. Phase 2: It explains the rubber compound's curing properties. Phase 3: It provides an excellent indication of the rubber compound's physical characteristics. According to E. Ateia et al. [7], one may infer from the figure important parameters that are in charge of the changes that take place during the vulcanization process.

2.3 Characterizations and measurements

X-ray diffraction (analytical-x'pert pro, Cu K$_{\alpha 1}$radiation, $\lambda = 1.5404$ Å, 45 kV, 40 mA, Netherlands) was used to detect the phase formation. FT-IR spectrometers were used to measure Fourier transformed infrared (FT-IR) spectra in the wavenumber range of 4000–400 cm^{-1} (PerkinElmer 2000). For the morphological investigation, a HRTEM (HRTEM, JEOL/JME 2100) (TEM, JEOL, JSM 7001F) microscope and Field Emission Scanning Electron Microscope (FESEM, model Quanta 250) were employed. X-ray photoelectron spectroscopy (XPS) was utilized to analyze the chemical states of various elements in the produced samples using monochromatic X-ray Al K-alpha radiation. Magnetic properties were discussed through vibrating-sample magnetometer. All tests for the mechanical parameters were conducted at a room temperature (25 °C). An average of 4 samples was taken for each measurements point.
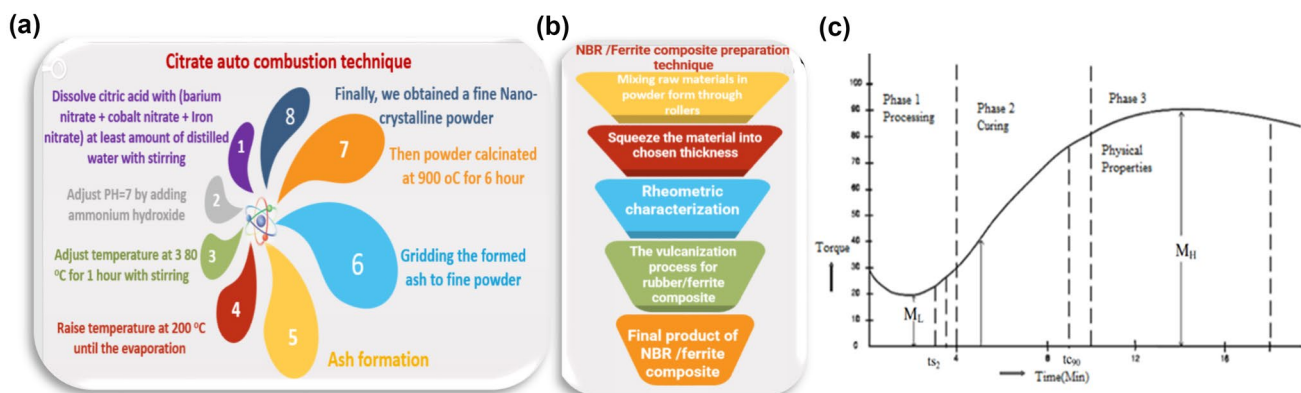

Fig. 2 a–c Schematic of preparation method for BFCO and 50NBR/50BFCO nanocomposites, **c** A typical Cure Curve

3 Results and discussion

3.1 Structure analyses

3.1.1 XRD diffraction

Figure 3 shows the XRD patterns in which all indexed peaks of the graph of BFCO and NBR/BFCO correspond to ICDD card number [00-043-002] of $BaFe_{12}O_{19}$. It indicates that the prepared samples are in single-phase without impurities. The 50% NBR/50% BFCO pattern appears to be a combination of the BFCO and NBR patterns, with humping between 15° and 25°.

The main diffraction peaks of NBR/BCFO are quite similar to the reflections from the as-prepared BCFO, indicating that the NBR coating does not cause any phase transition. However, due to the existence of the NBR coating layer, the intensity of the peaks for NBR/BCFO is weaker than that of the parent sample, which indicates that both samples have been successfully prepared.

The lattice parameters (a, c) and volume (V) are calculated from the XRD pattern, and the crystallite size (D) is calculated from the Scherrer equation [7], and the obtained data are tabulated in Table 1.

$$\frac{1}{d^2} = \frac{4}{3}\left(\frac{h^2+hk+k^2}{a^2}\right) + \frac{l^2}{c^2} \tag{2}$$

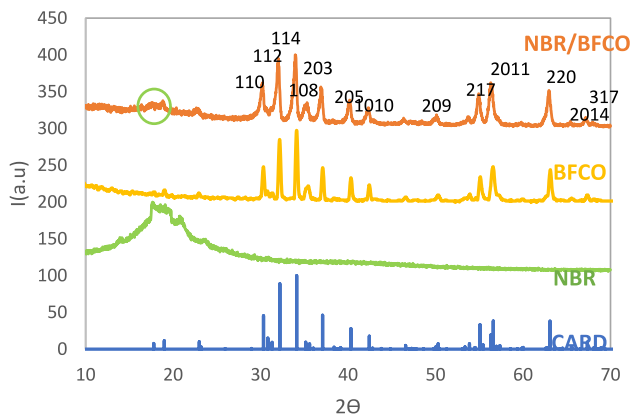$$V_{cell} = \frac{\sqrt{3}}{2}a^2c \tag{3}$$

$$D = \frac{k\lambda}{\beta\cos\theta} \tag{4}$$

The dislocation density δ is calculated for BFCO as an individual and mixed state, which is an indication of dislocations in the unit cell. The δ is obtained by following equation $\delta = 1/D^2$ and listed in Table 1.

It is found that NBR increases the c/a and the V_{cell}. This may be due to the crystal structure of $BaFe_{11.5}Co_{0.5}O_{19}$ being distorted after the addition of NBR. This structural deformation (stretching) may be explained by the change of diffraction angle (2Θ) toward small values (Fig. 3) as well as the value of δ.

3.1.2 Fourier transform infrared (FTIR)

Figure 4 reveals FT–IR spectra of rubber ferrite samples, pure NBR polymer and BFCO nano-powder samples in the wave number range of 200–4000 cm^{-1}. From the pattern, it is observed that the main absorption bands of HF appear between 400 and 600 cm^{-1} which is related to the stretching vibration of metal–oxygen in M-type HF for octahedral (B) and tetrahedral (A) sites, respectively [8]. The lower wavenumber peak is due to the stretching vibration of Fe–O in the B site. Other two peaks are due to the metal–oxygen stretching vibration in the A site.
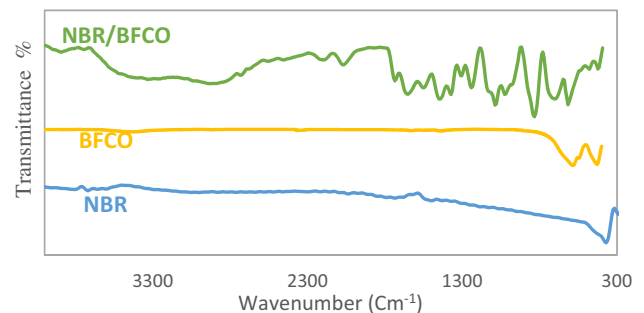

Fig. 3 XRD Diffraction pattern of pure NBR, BFCO and NBR/BFCO nanocomposite

Fig. 4 FTIR of NBR, BFCO and NBR/BFCO nanocomposites

Table 1 Lattice parameters (a and c), c/a ratio, crystallite size D, Dislocation density (δ) and, theoretical Density (d_x) of BFCO and NBR/BFCO

Sample	Theoretical values			Calculated values						
	a (A°)	c (A°)	V(A°)^3	a (A°)	c (A°)	V(A°)^3	c/a	D (nm)	δ 10^{-4} (nm^{-2})	d_x (g.Cm^{-3})
BFCO	5.889	23.187	696.55	5.889	23.187	696.531	3.937	36.78	7.392	5.306
NBR/BFCO	5.889	23.187	696.55	5.871	23.413	698.988	3.987	35.936	7.744	3.555

According to the relevant investigation, these two specific absorption peaks are the typical fingerprint of the formation for M-type barium hexaferrites.

The peaks at 1874, 1550 cm^{-1} are due to N$^+$–H stretching and bending frequencies, respectively [10]. While the peaks at 1442 cm^{-1}, 2198, 3635 cm^{-1}, 1640 cm^{-1} are due to C-H scissoring frequency [11], nitrile stretching frequency [12], OH groups, and OH bending, respectively [13].

Additionally, the detected peak at 2893 cm^{-1} can be attributed to the symmetric stretching vibration of methylene groups [14]. The observed peaks 3402, 3332, 3255, 3255, 1373, 1311, 1087, 1026, 655 indicate hydroxyl compound (OH) [16], On the other hand, the observed peaks at 1651,1734, 2731, and 2075 Cm^{-1} are due to double bond carbon C=C, carboxylic acid (steric acid), aldehyde, and Transition metal carbonyls frequencies, respectively [15]. All observed peaks are corresponding to compounds of HF/NBR composites, and no foreign peak is detected.

3.1.3 Raman spectroscopy (RS)

Figure 5 displays the RS of BFCO, NBR, and NBR/BFCO obtained at room temperature in the range of 200–800 cm^{-1}. On the basis of D$_{6h}$ symmetry, group theory analysis of hexaferrites yields 42 Raman active modes, which are dispersed in the form of irreducible representation as $14E_{1g} + 17E_{2g} + 11A_{1g}$ [16]. Raman modes have been detected at 200, 316, 404, 468, 504, 602, and 671 cm^{-1}. The modes at 316, 404, 504, 602, and 671 cm^{-1} correspond to vibrations of the 12 k and 2a octahedral sites, the 4f$_2$ B site, and the 2b bi-pyramidal site, respectively, due to A$_{1g}$, E$_{1g}$, A$_{1g}$, A$_{1g}$, and A$_{1g}$ symmetry [17].

The NBR rubber is identified, and its characteristic band appears at $\cong$ 496 Cm^{-1} corresponding to C=C$_2$ rocking and

scissoring [18], and 463, 237 Cm^{-1} corresponding to deformation (C=C–C) and torsion (C–C), respectively [19].

Figure 5b illustrates the imaging of a substrate through RS, in the case of the NBR/BFCO nanoparticles. Good adhesion and high homogeneity between phases of the nanocomposite are observed.

3.1.4 XPS analysis

XPS is a very effective technique for quantitatively investigating the components present in a substance. This powerful approach may be used to investigate the composition and state of the elements, as well as the electronic structure and density of the states in the material. XPS measurements are utilized in the present work to investigate the chemical states of each element in BFCO. Figure 6a shows the BFCO whole-range XPS survey spectrum at energies ranging from 0 to 1200 eV.

Only C, Ba, Fe, Co, and O peaks are detected. The C 1 s peak at 286.24 eV is caused by contaminating carbon. [20, 21]. The element binding energy shows that the BFCO hexaferrites are single-phase with no extra impurity phases. The survey scan spectra Fig. 6a revealed peaks of Fe 2p, Ba 3d, Co 2p, and O 1 s in the material. The binding energies of the Ba 3d$_{5/2}$ and Ba 3d$_{3/2}$ peaks are 779.62 and 794.74 eV, respectively, [20] as shown in Fig. 6b.

Two distinct significant Fe peaks are observed and depicted in Fig. 6c. The first significant peak (2p$_{3/2}$) is separated into two peaks, one at 710.52 eV and the other at 712.86 eV [22, 23].

The first peak is associated with the Fe^{2+} state, whereas the second one is associated with the Fe^{3+} state. There are also two satellite peaks at 716.53 eV and 719.57 eV [21]. The second main peak (2p$_{1/2}$) is likewise separated into two peaks, each at 724.14 eV, and 727.36 eV [21]. The first peak
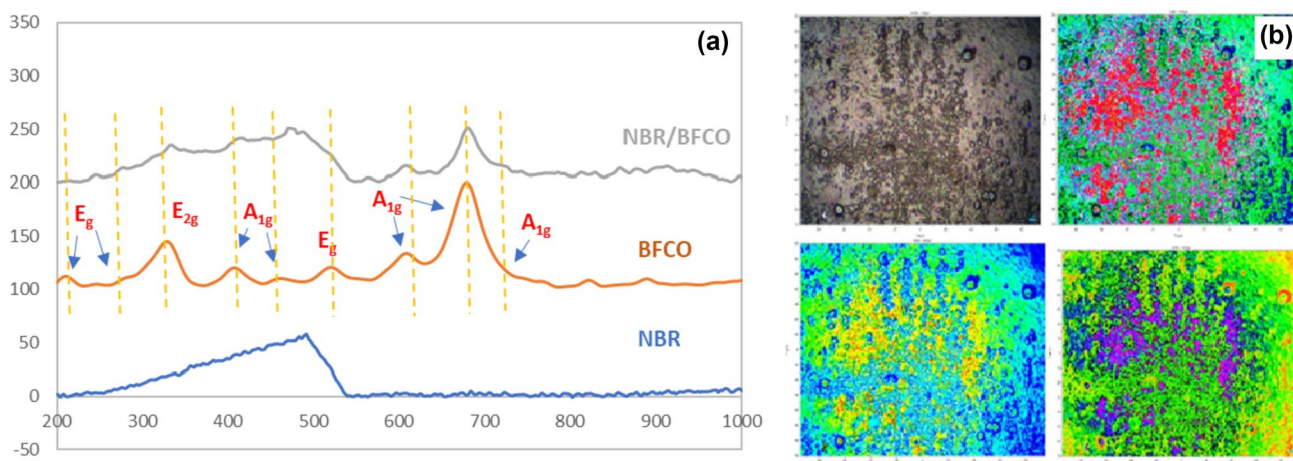

Fig. 5 **a**–**b** Raman spectra for BFCO, NBR and 50% NBR/50% BFCO **b** optical micrographs of NBR/BFCO nanocomposites
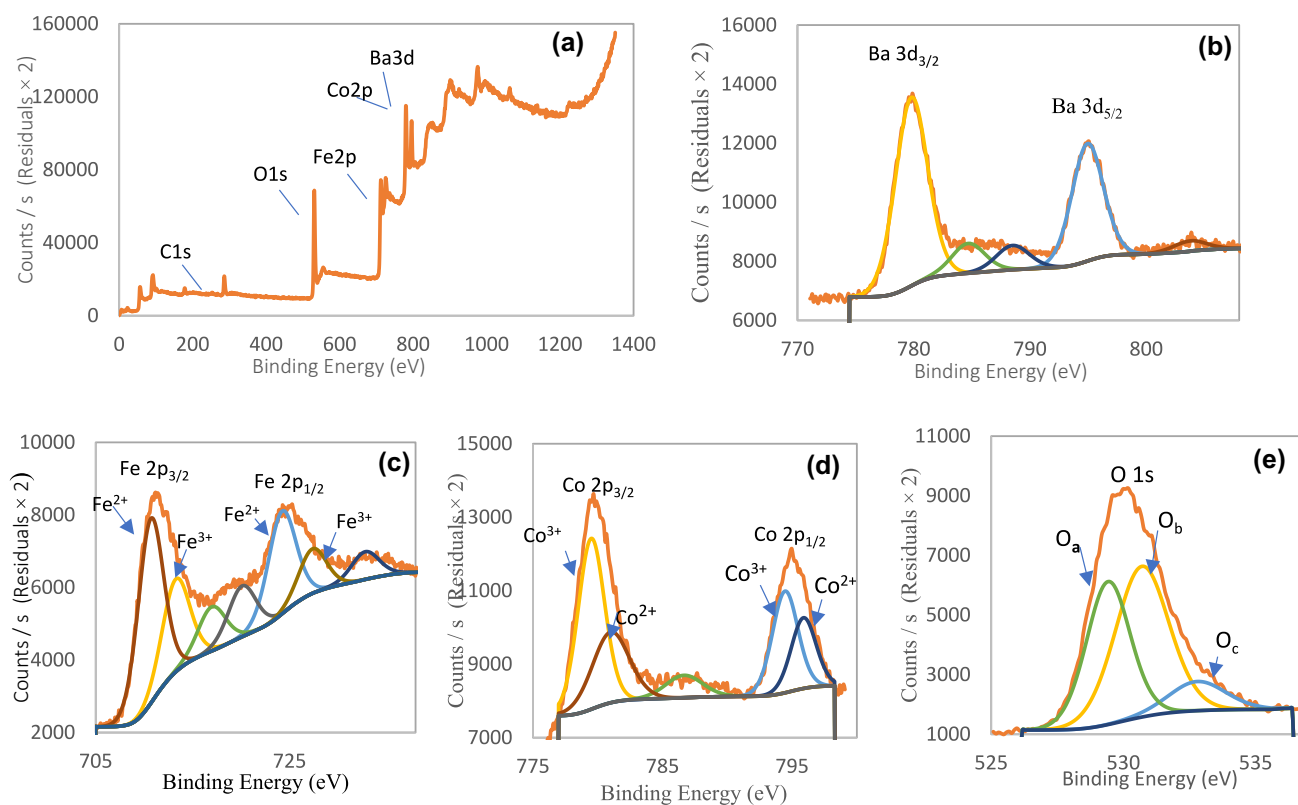
Fig. 6 XPS spectra of the BFCO **a** full range XPS survey spectrum, **b** high-resolution spectrum for Ba 3d, **c** high-resolution spectrum for Fe 2p, **d** high-resolution spectrum for Co 2p, and **e** high-resolution spectrum for O 1 s

corresponds to the Fe^{2+} state, whereas the second corresponds to the Fe^{3+} state. At 732.81 eV, more satellite peaks cantered [21, 24]. Figure 6d reveals two significant peaks at 779.8 eV and 794.95 eV, which relate to Co^{2+} $2p_{3/2}$ and Co^{2+} $2p_{1/2}$, respectively [25]. The existence of Fe^{2+} and Co^{3+} ions may imply a charge transfer between Fe and Co ions ($Fe^{3+} + Co^{2+} \Leftrightarrow Fe^{2+} + Co^{3+}$) [26]. Figure 6e shows characteristic peak of O 1 s, and this peak has been separated into three separate peaks. The peak at 529.42 eV (O_a) is attributed to intrinsic O^{2-} ions, and the peak at 532.8 eV (O_c) is ascribed to an adsorbed O^{2-} ions during sample processing [21, 24]. The peak at 530.7 eV (O_b) is caused by oxygen vacancies [27], and the concentration of oxygen vacancies is frequently estimated using (O_b/O_{total}) [21].

3.1.5 Microstructural features

HRTEM images of hexaferrite sample particles with of various sizes and shapes are shown in Fig. 7. The particles are typically hexagonal with rectangular shapes that match the hexaferrite structure [28]. The well-defined crystalline nature and single-phase nano-BFCO hexaferrites are shown by selected area electron diffraction (SAED) Fig. 7b.

The data are fitted to a Gaussian distribution, and the average particle size of the samples is 90.

Figure 8a–e shows SEM micrographs of pure NBR, BFCO and NBR/BFCO. A rough morphology is observed for pure NBR Fig. 8a, as expected. The nanocomposites morphology is characterized by a two-phase structure in which one component is dispersed in the other, forming a continuous matrix as detected in Fig. 8b–d. The morphology of the two phases indicates that the interaction between the ferrite and rubber improves their adherence to one other. A few cavities, cracks, and pores can be found between the ferrite and rubber systems, proving the system's homogeneity. The SEM images correspond well with the RS results.

3.1.6 Surface topography using AFM

AFM pictures of 50NBR/50BFCO nanocomposites are shown in Fig. 9a–b. The physical dimensions and thickness of the nano-samples can be easily derived from the profile of height. The average roughness (Ra) values for BFCO and 50BFCO/50NBR are 2.45 nm and 3.15 nm, respectively. The root mean square (Rq) values for BFCO and 50NBR/50BFCO are 3.33 nm and 4.28 nm, respectively.

The three-dimensional picture presented in Fig. 9a–b also records the distribution of particles on the surface. Two-dimensional structures have a maximum valley depth
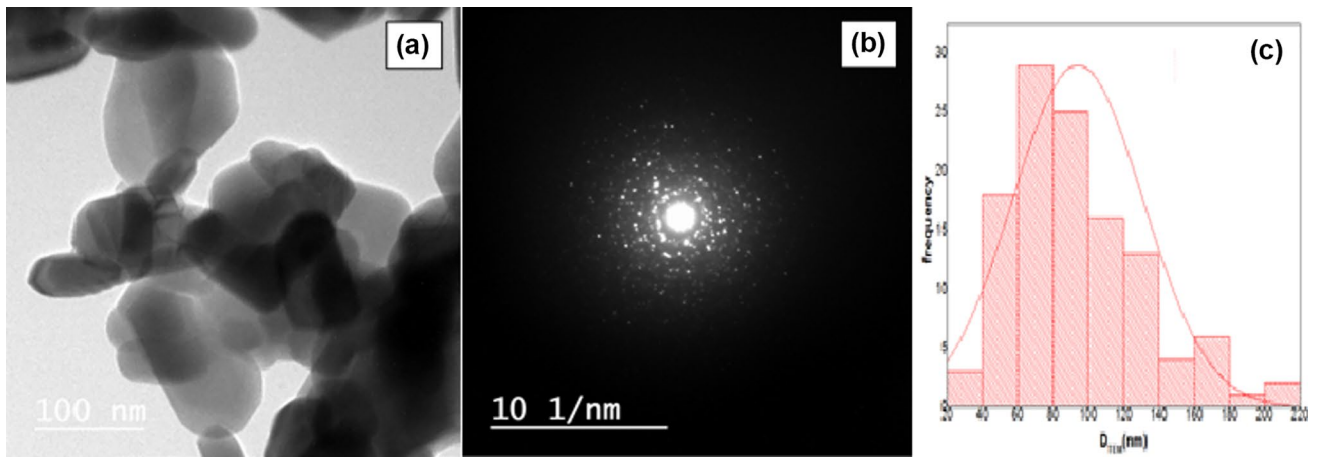
Fig. 7 **a–c a** HRTEM micrographs **b** selected area electron diffraction, and **c** of BFCO hexaferrite samples
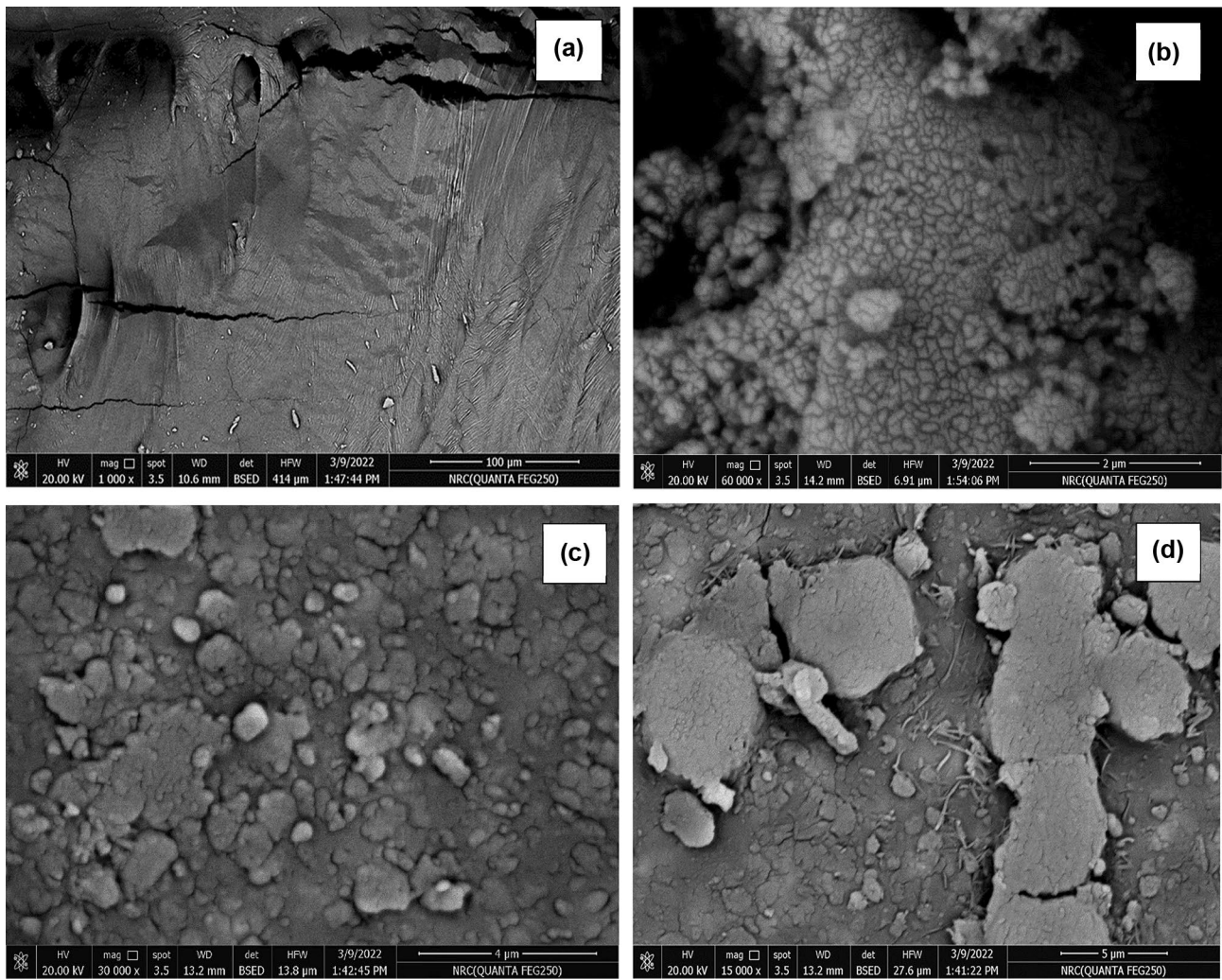

Fig. 8 **a–d** SEM micrographs of pure NBR, BFCO and NBR/BFCO
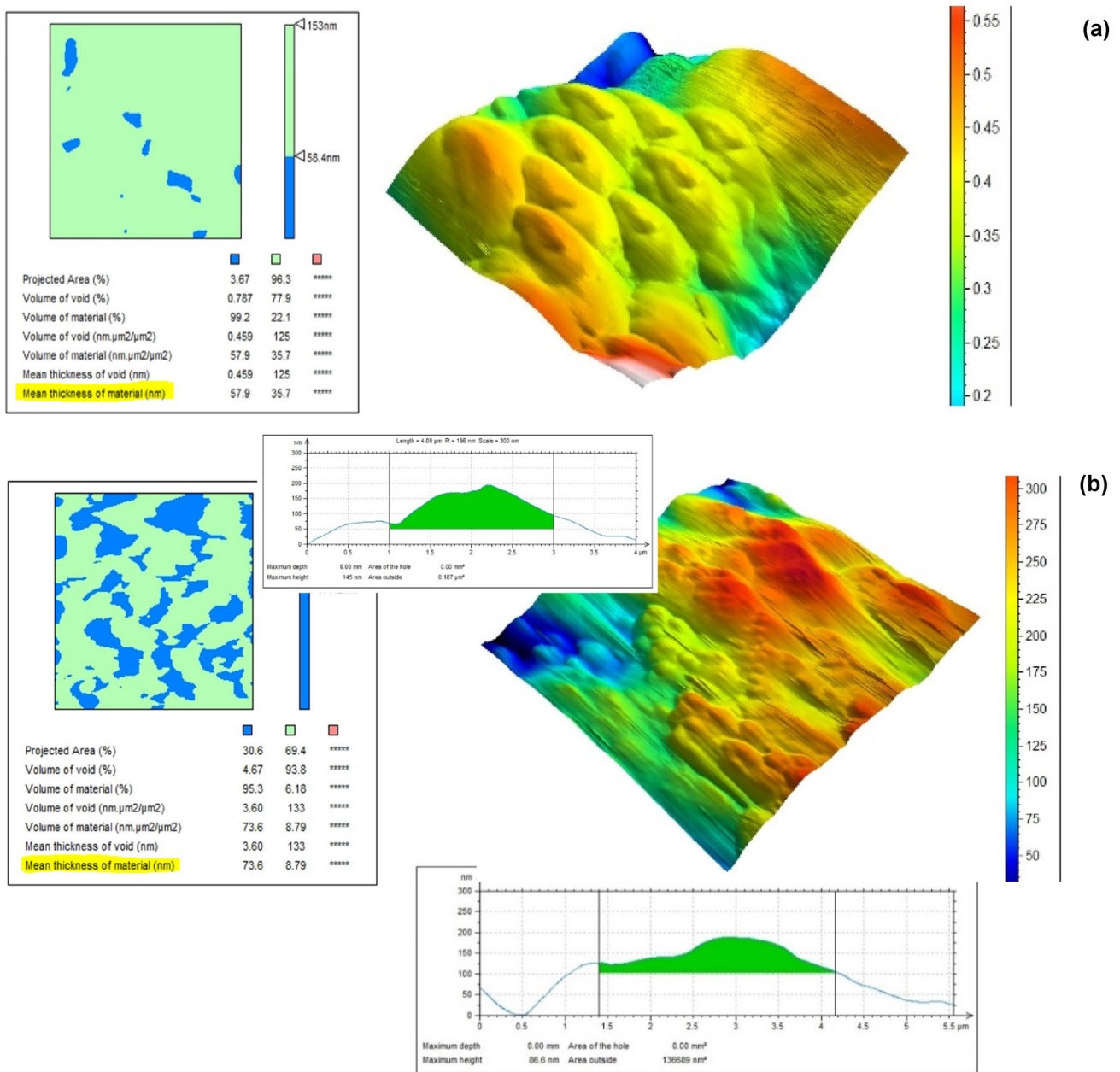
Fig. 9 a–b AFM images for grain boundaries with comparable grain sizes for two samples of BFCO and NBR/BFCO

of for BFCO and NBR/BFCO are 13.1 nm and 13.9 nm, respectively.

3.2 Magnetic measurements

3.2.1 VSM hysteresis loop

Figure 10a–d depicts the hysteresis loops of BFCO, NBR, and NBR/BFCO. The magnetization performance of BFCO and NBR/BFCO is comparable to that of hard magnetic materials [29]. The obvious M–H loops in Fig. 10a, c

implies that BFCO & NBR/BFCO samples possess ferromagnetic characteristics, which should be attributed to the existence of BFCO NPs. The magnetic parameters such as saturation magnetization (M_s), coercivity (H_c) and remanent magnetization (M_r) are listed in Table 2.

Compared with pure BFCO, a significant decline in Ms and Mr values in the nano-composites samples can be ascribed to the decrease in the weight ratio of BFCO by adding NBR, as shown in Table 2 [30].

The Fe^{3+}–O–Fe^{3+} super-exchange interaction in the current system can explain the high Ms values for BFCO.
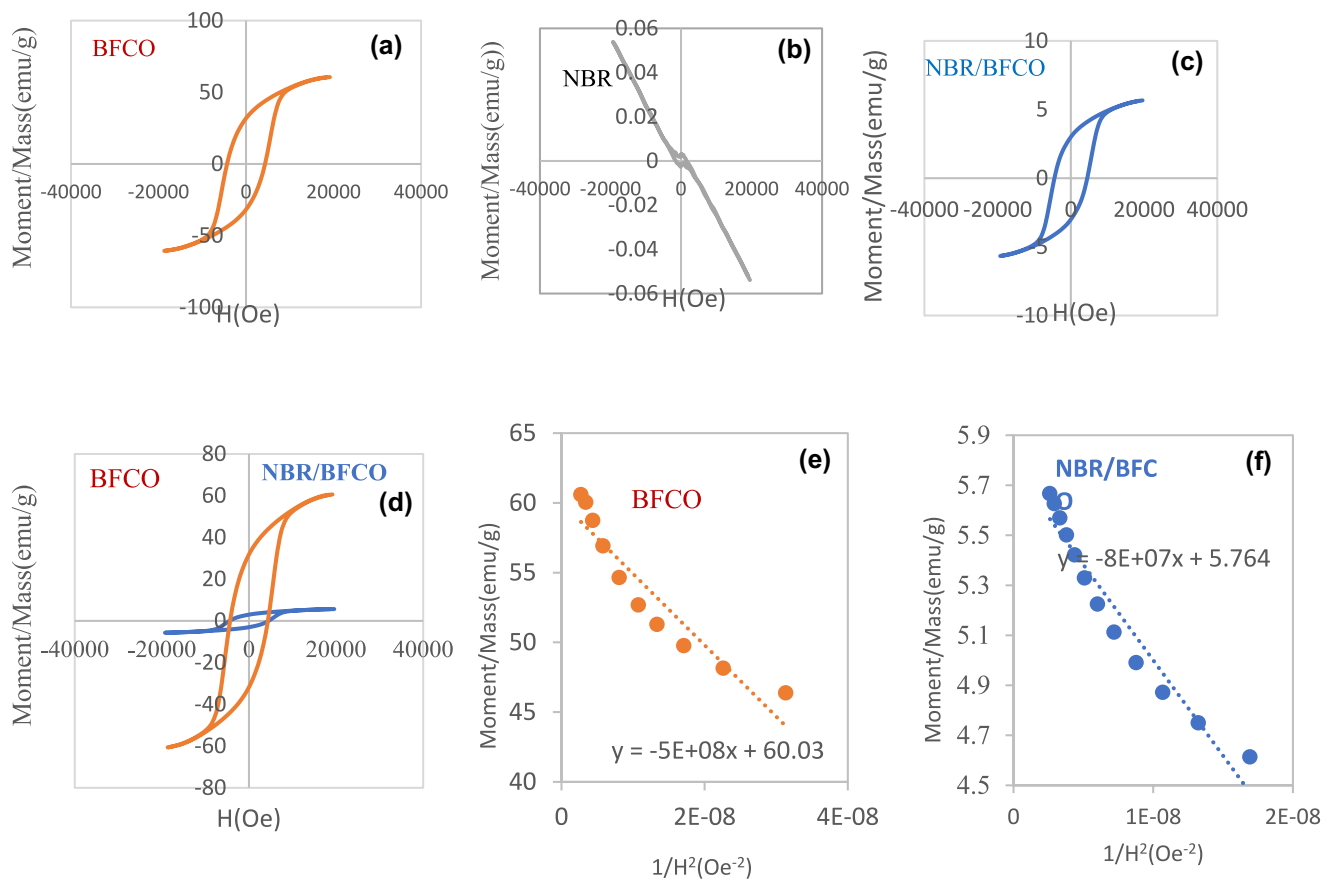
Fig. 10 **a–d** Magnetic hysteresis loops for BFCO, NBR and NBR/BFCO. **e–f** Fitting plot between M versus 1/H^2 for BFCO and NBR/BFCO

Table 2 The area of the hysteresis loop, coercivity (H$_c$), saturation magnetization (M$_s$), remanent magnetization (M$_r$), exchange bias (EB), Squareness (M$_r$/M$_S$), the effective anisotropy constant (K$_{eff}$) and the anisotropy field (Ha)

Magnetic parameters	Area (erg/g) 10^3	H$_c$ (Oe)	M$_s$ (emu/g)	(M$_r$) (emu/g)	EB (Oe)	M$_r$/M$_S$	K$_{eff}$ (emu Oe g^{-1}) $\times 10^3$	Ha (Oe) $\times 10^3$
BFCO	665.300	4341	60.03	31.810	4.75	0.533	2599	87.170
50BFCO/50NBR	65.109	4462	5.764	3.001	2.6	0.529	99.8	35.238

An investigation has found that substitution in M-type hexaferrite systems alters the valence states of Fe^{3+} ions to Fe^{3+} ions at the 2A sites [31]. This causes an enhancement of super-exchange interactions that improves the hyperfine field at 2b and 12 k sites. Additionally, the dissimilarity of ionic radius between Co^{2+} (0.74 A°) and Fe^{3+} (0.64 A°) will affect the distance between different ions and consequently lead to strengthening the super-exchange interaction. Likewise, the preferred site occupancy of the substituted ions has a significant impact on the Ms values [32, 33]

Based on the Stoner–Wohlfarth (S–W) approach, the saturation magnetization (Ms) values can be deduced by extrapolating curves of M vs 1/H^2 to approach 0 [32, 33].

Plots of M vs 1/H^2 for 50 BCFO/50NBR hexa-nanoferrites are illustrated in Fig. 10a–f.

It is noticeable that the nano-hexaferrites exhibit Mr/Ms values around 0.5, which indicates the uniaxial anisotropy for the prepared samples according to the S–W approach [32, 33]. We note that the values of Ms are estimated via the following expression [32, 33]:

$$M = Ms\left[1 - \frac{\beta}{H^2}\right] \qquad (5)$$

Consequently, β is a constant that relates to the magnetocrystalline anisotropy. The effective anisotropy constant (K$_{eff}$) can be deduced as follows [32, 33]:

$$K_{eff} = Ms \left[\frac{15\beta}{4} \right]^{1/2} \tag{6}$$

The K_{eff} varies due to changes in magnetic anisotropy sources such as shape and surface anisotropies, as well as the strengthening (or weakening) of magnetic interaction among NPs. The addition of NBR with BCFO composites is the main causes for the detected change.

The anisotropy field (Ha) can be determined as follows [32]:

$$Ha = \frac{2K_{eff}}{M_s} \tag{7}$$

The calculated values of Ha are large, which implies that our produced composites are magnetically hard. From the table, it is noticeable that the Hc values are slightly increased by the addition of NBR compared to parent BCFO hexaferrite. It is highest for BCFO hexaferrite with values around 4341 and 4462 Oe, for BCFO and BCFO/NBR, respectively. The increase in Hc is due to the defects in the composition and polymerization processes, which may act as pinning centers during the magnetization reversal process [33]. Additionally, the interaction between the BCFO and NBR will change the surface charge density and the electron spin mechanism of the BCFO NPs and also reduce the resistance of the domain wall displacement of the BCFO in the NBR/BCFO. This increase in NBR-coated BCFO suggests that the prepared nanocomposite products could be very promising candidates for a wide range of magnetic and mechanical applications. The Hc is intrinsically influenced by particle size, composition, defects, and the exchange interaction [34]. Moreover, the contribution of magneto-crystalline anisotropy to Hc is dominant in hard magnetic NPs. It cannot be ignored, as it was in the case of soft ferromagnetic nanoparticles.

3.2.2 The switching field distribution (SFD)

The SFD is defined by the following equation, which is another essential magnetic characteristic [35].

$$SDF = \frac{\Delta H}{H_C} \tag{8}$$

where ΔH denotes the full width at half maximum of the differentiated curve dM/dH shown in Fig. 11a–b). SDF equals 4636, and 4876 for BFCO and NBR/BFCO, respectively. This value represents the energy barrier distribution in a nanoparticle system, which is accompanied by a particle coercivity distribution. In general, the SFD is linked to recording characteristics such as optimal bias current and noise.

The derivative curves give useful information on the magnetic characteristics of the system. The formation of two peaks in SFD, on the other hand, indicates a competition between strong dipolar interactions and exchange coupling [35].

3.3 Rheometric and mechanical measurements

However, the mechanical parameters of the studied samples are checked after vulcanization at tc_{90}. For the evaluation of the mechanical parameters of the examined NBR/BFCO, tensile strength (TS), elongation at break (EB), modulus (E), and hardness (H) are tabulated in Table 3. The addition of 50% weight of $BaFe_{11.5}Co_{0.5}O_{19}$ with 50% weight of EPDMNBR increases the mechanical parameters compared to the pure NBR samples. The addition of BFCO with NBR matrix increases the cross-linking between rubber molecules, reducing their mobility and thus increasing the modulus and strength [7]. At the same time, refining the "H" and other mechanical parameters. The results indicate that the
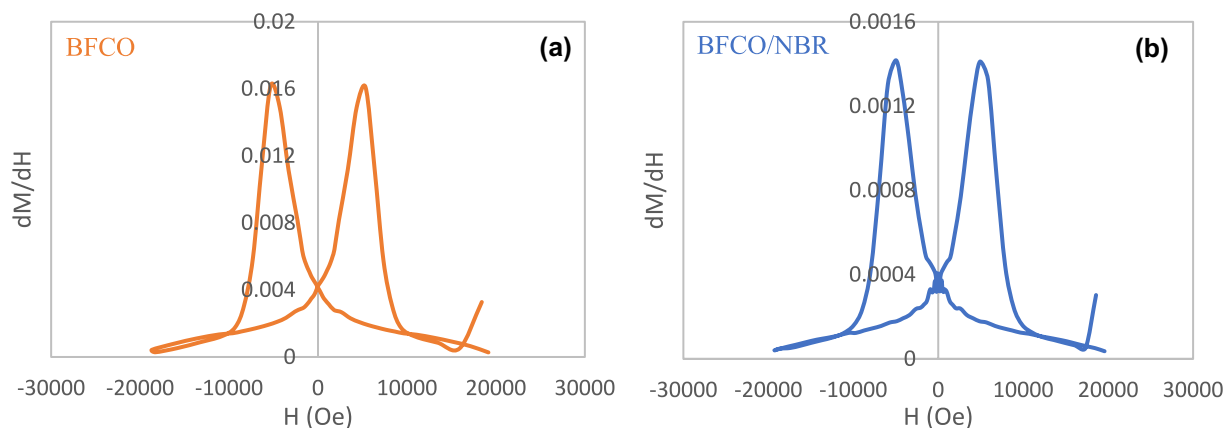

Fig. 11 a–b Switching field distribution for **a** BFCO **b** NBR/BFCO

Table 3 M$_L$ (minimum torque), M$_H$ (maximum torque), ts$_2$ (scorch time), tc$_{90}$ (optimum cure time), cure rate index (CRI), tensile strength (T.S), young's modulus (E) and hardness (H)

Parameter	M$_L$ (dN.m)	M$_H$ (dN.m)	ts$_2$ (Min)	tc$_{90}$ (Min)	CRI(Min^{-1})	T.S (MPa)	E (%)	H (shore A)
NBR	3	50	3	8	16.67	3.48	500	55
NBR/BFCO	7	65	6.5	11	22.22	7.25	700	70

BFCO ferrite NPs act as good reinforcing material for NBR. This is due to the homogeneous dispersion of ferrite NPs in NBR matrix, which leads to an increase in the interfacial forces between ferrite and rubber. This can be attributed to the homogeneous dispersion of ferrite nanoparticles in NBR matrix, increase in the interfacial forces between BaFe$_{11.5}$Co$_{0.5}$O$_{19}$ and NBR.

The Torque values such as M$_L$ (Minimum Torque) and M$_H$ (Maximum Torque), Time values such as ts$_2$ (Scorch time) and tc$_{90}$ (optimum cure time), Cure Rate Index (CRI), Tensile strength (T.S), Young's modulus (E) and hardness (H) are enhanced after the addition of BFCO nanoparticles to NBR polymer listed as detected in Table 3.

4 Conclusion

The major goal of this study is to improve the physical properties of the investigated composites and yield obtaining hard magnetic materials with good mechanical properties to get more applicable material. The obtained data indicate that the Ba Co$_{0.5}$Fe$_{11.5}$O$_{19}$ nanoferrites act as good strengthening material for NBR. The addition of 50% weight of hexaferrite with 50% weight of NBR increases the mechanical parameters compared to the pure NBR samples. The originality of this investigation is clarified from emphasizing the magnetization of NBR and to accentuate the good mechanical properties of the investigated nanocomposites.

The addition of NBR with BCFO composites decreases the effective anisotropy constant (K_{eff}) due to changes in magnetic anisotropy sources such as shape and surface anisotropies, as well as the strengthening (or weakening) of magnetic interaction among NPs.

Finally, the preparation of magnetic material (Ba Co$_{0.5}$Fe$_{11.5}$O$_{19}$) with a polymer (NBR) allowed for the creation of a nanocomposite that possesses mechanical as well as magnetic properties, opening variety of applications.

Author contributions EEA contributed to experimentation, writing the original manuscript, reviewing and editing the final manuscript, and supervision. KE contributed to material preparation, data collection and analysis, optimum selection of material parameters, experimentation, editing, validation and visualization. DEE-N contributed to experimentation, review and editing.

Declarations

Conflict of interest The authors declare that they have no known competing financial interests or personal relationships that could have appeared to influence the work reported in this paper.

Ethical approval Not applicable.

References

1. D.E. El-Nashar, N.M. Ahmed, W.R. Agami, The effect of new ferrite/kaolin pigment on the properties of acrylonitrile–butadiene rubber composites. Mater. Des. **1980–2015**(52), 108–117 (2013). https://doi.org/10.1016/j.matdes.2013.05.047

2. G. Benito, M.P. Morales, J. Requena, V. Raposo, M. Vázquez, J.S. Moya, Barium hexaferrite monodispersed nanoparticles prepared by the ceramic method. J. Magn. Magn. Mater. **234**, 65–72 (2001). https://doi.org/10.1016/S0304-8853(01)00288-8

3. C. Wu, Z. Yu, K. Sun et al., Calculation of exchange integrals and Curie temperature for La-substituted barium hexaferrites. Sci. Rep. **6**, 36200 (2016). https://doi.org/10.1038/srep36200

4. H. Nikmanesh, M. Moradi, G.H. Bordbar, R. Shams Alam, Efect of multi dopant barium hexaferrite nanoparticles on the structural, magnetic, and X-Ku bands microwave absorption properties. J. Alloys Compd. **708**, 99–107 (2017). https://doi.org/10.1016/j.jallcom.2017.02.308

5. K.A. Malini, E.M. Mohammed, S. Sindhu, P. Kurian, M.R. Anantharaman, Dielectric and mechanical properties of rubber ferrite composites. Plast. Rubber Compos. **31**, 449–457 (2002). https://doi.org/10.1179/146580102225006396

6. C. Singh, E.E. Ateia, S.B. Narang, M. Farag, J. Singh, D.E. El-Nashar, Development of Co$_{0.7}$Ca$_{0.3}$Fe$_2$O$_4$-EPDM nanocomposite

for microwave application: Their rheometric behavior, surface topography and electromagnetic parameters. Ceram. Int. **47**, 7285–7290 (2021). https://doi.org/10.1016/j.ceramint.2020.11.034

7. E.E. Ateia, D.E. El-Nashar, R. Ramadan et al., Synthesis and characterization of EPDM/ferrite nanocomposites. J. Inorg. Organomet. Polym. **30**, 1041–1048 (2020). https://doi.org/10.1007/s10904-019-01237-6

8. P. Dipak, D.C. Tiwari, S.K. Dwivedi, Synthesis of polymer blend ferrite composite for microwave absorption at X-band frequency. J. Metal **9**(4), 33–41 (2019)

9. S. Kolev, B. Georgieva, T. Koutzarova, K. Krezhov, C. Ghelev, D. Kovacheva, B. Vertruyen, R. Closset, L.M. Tran, M. Babij, A.J. Zaleski, Magnetic field influence on the microwave characteristics of composite samples based on polycrystalline Y-type hexaferrite. Polymers **14**, 4114 (2022). https://doi.org/10.3390/polym14194114

10. E.E. Ateia, K. Elsayed, R. Ramadan, Tuning the properties of ba-m hexaferrite $BaFe_{11.5}Co_{0.5}O_{19}$: a road towards diverse applications. J. Inorg. Organomet. Polym. **32**, 2502–2512 (2022). https://doi.org/10.1007/s10904-022-02341-w

11. C. Thirupathy, S.C. Lims, S.J. Sundaram, A.H. Mahmoud, K. Kaviyarasu, Equilibrium synthesis and magnetic properties of BaFe12O19/NiFe2O4 nanocomposite prepared by co precipitation method. J. King Saud Univ. Sci. **32**, 1612–1618 (2020). https://doi.org/10.1016/j.jksus.2019.12.019

12. S. Sadhu, A.K. Bhowmick, Effect of chain length of amine and nature and loading of clay on styrene-butadiene rubber-clay nanocomposites. Rubber Chem. Technol. **76**, 860–875 (2003). https://doi.org/10.5254/1.3547777

13. A. Sattar, D. El-Nashar, W. Agami, M.A. Aly, Mechanical and dielectric properties of cobalt–zinc nanoferrite/nitrile butadiene rubber composites. J. Thermoplast. Compos. Mater. **31**, 3–22 (2018). https://doi.org/10.1177/0892705716632864

14. S. Chakraborty, S. Bandyopadhyay, R. Ameta, R. Mukhopadhyay, A.S. Deuri, Application of FTIR in characterization of acrylonitrile-butadiene rubber (nitrile rubber). Polym. Test. **26**, 38–41 (2007). https://doi.org/10.1016/j.polymertesting.2006.08.004

15. S. Sadhu, A.K. Bhowmick, Preparation and properties of nanocomposites based on acrylonitrile–butadiene rubber, styrene–butadiene rubber, and polybutadiene rubber. J. Polym. Sci. B Polym. Phys. **42**, 1573–1585 (2004). https://doi.org/10.1002/polb.20036

16. B. Mensah, K. Chandra Gupta, G. Kang, H. Lee, C. Nah, A comparative study on vulcanization behavior of acrylonitrile-butadiene rubber reinforced with graphene oxide and reduced graphene oxide as fillers. Polym. Test. **76**, 127–137 (2019). https://doi.org/10.1016/j.polymertesting.2019.01.026

17. A. Nandiyanto, R. Oktiani, R. Ragadhita, How to read and interpret FTIR spectroscope of organic material. Indones. J. Sci. Technol. **4**, 97–118 (2019). https://doi.org/10.17509/ijost.v4i1.15806

18. K. Rana, P. Thakur, M. Tomar, V. Gupta, A. Thakur, Investigation of cobalt substituted M-type barium ferrite synthesized via co-precipitation method for radar absorbing material in Ku-band (12–18GHz). Ceram. Int. **44**, 6370–6375 (2018). https://doi.org/10.1016/j.ceramint.2018.01.028

19. S. Kumar, M.K. Manglam, S. Supriya, H.K. Satyapal, R.K. Singh, M. Kar, Lattice strain mediated dielectric and magnetic properties in La doped barium hexaferrite. J. Magn. Magn. Mater. **473**, 312–319 (2019). https://doi.org/10.1016/j.jmmm.2018.10.085

20. S. Prasertsri, F. Lagarde, N. Rattanasom, C. Sirisinha, P. Daniel, Raman spectroscopy and thermal analysis of gum and silica-filled NR/SBR blends prepared from latex system. Polym. Test. **32**, 852–861 (2013). https://doi.org/10.1016/j.polymertesting.2013.04.007

21. S.W. Cornell, J.L. Koenig, The raman spectra of polybutadiene rubbers. Rubber Chem. Technol. **43**, 322–332 (1970). https://doi.org/10.5254/1.3547257

22. V.N. Archana, M. Mani, J. Johny, S. Vinayasree, P. Mohanan, M.A. Garza-Navarro, S. Shaji, M.R. Anantharaman, On the microwave absorption of magnetic nanofluids based on barium hexaferrite in the S and X bands prepared by pulsed laser ablation in liquid. AIP Adv. **9**, 035035 (2019). https://doi.org/10.1063/1.5088080

23. G.A. Alna'washi, A.M. Alsmadi, I. Bsoul, B. Salameh, G.M. Alzoubi, M. Shatnawi, S.M. Hamasha, S.H. Mahmood, Investigation on X-ray photoelectron spectroscopy, structural and low temperature magnetic properties of Ni–Ti co-substituted M-type strontium hexaferrites prepared by ball milling technique. Res. Phys. **28**, 104574 (2021). https://doi.org/10.1016/j.rinp.2021.104574

24. E.E. Ateia, M.A. Ateia, M.A. Fayed et al., Synthesis of nanocubic lithium cobalt ferrite toward high-performance lithium-ion battery. Appl. Phys. A **128**, 483 (2022). https://doi.org/10.1007/s00339-022-05622-w

25. M.A. Ateia, E.E. Ateia, M.M. Mohamed Mosry, Arman, Synthesis and characterization of non-stoichiometric $Li_{1.1}Co_{0.3}Fe_{2.1}O_4$ ferrite nanoparticles for humidity sensors. Appl Phys A **128**, 884 (2022). https://doi.org/10.1007/s00339-022-06030-w

26. G.A. Alnawashi, A.M. Alsmadi, I. Bsoul et al., Magnetic study of M-type Co-Ti doped strontium hexaferrite nanocrystalline particles. J. Supercond. Nov. Magn. **33**, 1423–1432 (2020). https://doi.org/10.1007/s10948-019-05334-y

27. E.E. Ateia, A. AL-Hamzi, B. Hussein, Synthesis and characterization of non-stoichiometric cobalt nanoferrites for multifunctional applications. J. Mater. Sci. **33**, 20642–20655 (2022). https://doi.org/10.1007/s10854-022-08876-5

28. F.M. Ahmed, E.E. Ateia, S.I. El-dek, S.M. Abd El-Kader, A.S. Shafaay, Silver-substituted cobalt zeolite imidazole framework on reduced graphene oxide nanosheets as a novel electrode for supercapacitors. J. Energy Storage **55**, 1054432022 (2022). https://doi.org/10.1016/j.est.2022.105443

29. E.E. Ateia, A.T. Mohamed, Core-shell nanoarchitectonics of $CoFe_2O_4$ encapsulated La2Fe2O6 nanoparticles for their use in various applications. J Inorg Organomet Polym **32**, 1389–1399 (2022). https://doi.org/10.1007/s10904-021-02202-y

30. J.Y. Kwak, C.S. Lee, D. Kim, Y.I. Kim, Characteristics of barium hexaferrite nanoparticles prepared by temperature-controlled chemical coprecipitation. J. Korean Chem. Soc. **56**, 609–616 (2012). https://doi.org/10.5012/jkcs.2012.56.5.609

31. M. Amini, A. Gholizadeh, Shape control and associated magnetic and dielectric properties of MFe12O19 (M=Ba, Pb, Sr) hexaferrites. J. Phys. Chem. Solids **147**, 109660 (2020). https://doi.org/10.1016/j.jpcs.2020.109660

32. A.V. Trukhanov, D.I. Tishkevich, Podgornaya, et al., Impact of the nanocarbon on magnetic and electrodynamic properties of the ferrite/polymer composites. Nanomaterials **12**, 868 (2022). https://doi.org/10.3390/nano12050868

33. S.J. Ouyang, D. Mu, Y. Zhang, H. Yang, S.L. Suib, Selective fabrication of barium carbonate nanoparticles in the lumen of halloysite nanotubes. Minerals **8**(7), 296 (2018)

34. M.A. Almessiere, Y. Slimani, H.S. El Sayed, A. Baykal, Structural and magnetic properties of Ce–Y substituted strontium nanohexaferrites. Ceram. Int. **44**, 12511–12519 (2018). https://doi.org/10.1016/j.ceramint.2018.04.045

35. M.A. Almessiere, Y. Slimani, A. Baykal, Structural and magnetic properties of Ce-doped strontium hexaferrite. Ceram. Int. **44**, 9000–9008 (2018). https://doi.org/10.1016/j.ceramint.2018.02.101

36. J.M. Wesselinowa, L. Apostolova, Size anisotropy and doping effects on the coercive field of ferromagnetic nanoparticles. J

Phys **19**, 406235 (2007). https://doi.org/10.1088/0953-8984/19/40/406235

37. E.E. Ateia, M. Farag, Synthesis of cobalt/calcium nanoferrites with controllable physical properties. Appl. Phys. A **125**, 324 (2019). https://doi.org/10.1007/s00339-019-2593-x

Publisher's Note Springer Nature remains neutral with regard to jurisdictional claims in published maps and institutional affiliations.